

# Weighted Abundance-Constrained Linear Spectral Mixture Analysis

Chein-I Chang, *Senior Member, IEEE*, and Baohong Ji, *Student Member, IEEE*

**Abstract**—Linear spectral mixture analysis (LSMA) has been used in a wide range of applications. It is generally implemented without constraints due to mathematical tractability. However, it has been shown that constrained LSMA can improve unconstrained LSMA, specifically in quantification when accurate estimates of abundance fractions are necessary. As constrained LSMA is considered, two constraints are generally imposed on abundance fractions, abundance sum-to-one constraint (ASC) and abundance nonnegativity constraint (ANC), referred to as abundance-constrained LSMA (AC-LSMA). A general and common approach to solving AC-LSMA is to estimate abundance fractions in the sense of least squares error (LSE) while satisfying the imposed constraints. Since the LSE resulting from each individual band in abundance estimation is not weighted in accordance with significance of bands, the effect caused by the LSE is then assumed to be uniform over all the bands, which is generally not necessarily true. This paper extends the commonly used AC-LSMA to three types of weighted AC-LSMA resulting from three different signal processing perspectives, parameter estimation, pattern classification, and orthogonal subspace projection. As demonstrated by experiments, the weighted AC-LSMA generally performs better than unweighted AC-LSMA which can be considered as a special case of our proposed weighted AC-LSMA with the weighting matrix chosen to be the identity matrix.

**Index Terms**—Abundance-constrained linear spectral mixture analysis (AC-LSMA), linearly constrained minimum variance (LCMV)-weighted AC-LSMA, Mahalanobis distance (MD), MD-weighted AC-LSMA, orthogonal subspace projection (OSP)-weighted AC-LSMA,  $S_W^{-1}$ -weighted AC-LSMA.

## I. INTRODUCTION

**L**INEAR spectral mixture analysis (LSMA) is a versatile technique which has shown success in solving a variety of problems [1], [2] such as subpixel detection [3]–[5], mixed-pixel classification [6]–[10], quantification [10]–[18], etc. It assumes that there are  $p$  image endmembers,  $\mathbf{m}_1, \mathbf{m}_2, \dots, \mathbf{m}_p$  present in an image to be processed, and any image pixel vector  $\mathbf{r}$  can be described as a linear mixture of these  $p$  endmembers with appropriate abundance fractions,  $\alpha_1, \alpha_2, \dots, \alpha_p$  with  $\alpha_j$  corresponding to the abundance fraction of the  $j$ th endmember  $\mathbf{m}_j$  as follows [8].

$$\mathbf{r} = \mathbf{M}\boldsymbol{\alpha} + \mathbf{n} \quad (1)$$

where  $\mathbf{n}$  is interpreted as a model or measurement error and  $\mathbf{M} = [\mathbf{m}_1 \ \mathbf{m}_2 \ \dots \ \mathbf{m}_p]$  is the endmember matrix formed by

$\mathbf{m}_1, \mathbf{m}_2, \dots, \mathbf{m}_p$ . Due to mathematical tractability, the LSMA is widely implemented as an unconstrained technique which does not impose any constraint on the abundance fractions  $\alpha_1, \alpha_2, \dots, \alpha_p$  of the image endmembers  $\mathbf{m}_1, \mathbf{m}_2, \dots, \mathbf{m}_p$ . However, it has been shown in the literature, e.g., [1], [5], [13], and [16], that constrained LSMA can improve unconstrained LSMA in many aspects such as subpixel detection [5], mixed-pixel classification [10], [13], [16], identification [19], specially quantification [13], [16], [18], [19] when accurate abundance fraction estimation is required. As constrained LSMA is considered, two abundance constraints can be imposed on  $\alpha_1, \alpha_2, \dots, \alpha_p$  in (1), abundance sum-to-one constraint (ASC), i.e.,  $\sum_{j=1}^p \alpha_j = 1$  and abundance nonnegativity-constraint (ANC),  $\alpha \geq \mathbf{0}$ , i.e.,  $\alpha_j \geq 0$  for all  $1 \leq j \leq p$ . Such constrained LSMA is referred to as abundance-constrained LSMA (AC-LSMA). A general and common approach to solving AC-LSMA is to estimate abundance fractions in the sense of least squares error (LSE) while satisfying the imposed constraints, which is referred to as LSE AC-LSMA. More specifically, the model in (1) is interpreted as least squares error problem

$$(\mathbf{r} - \mathbf{M}\boldsymbol{\alpha})^T (\mathbf{r} - \mathbf{M}\boldsymbol{\alpha}) \quad (2)$$

with  $\mathbf{n}$  is modeled as least squares error, while constraining the abundance fractions  $\alpha_1, \alpha_2, \dots, \alpha_p$  on the model in (2) to find least squares error solutions. As a result, three types of LSE AC-LSMA can be considered [1], [13], [16], sum-to-one constrained least squares (SCLS) which implements only the ASC, nonnegativity constrained least squares (NCLS) which implements only the ANC, and fully constrained least squares (FCLS) which implements both the ASC and the ANC [1], [13], [16]. Despite the fact that constrained LSMA may require more sophisticated algorithmic implementations, the pay-off is sometimes great and worthwhile, particularly, for material quantification [16], [19]. Most importantly, it generally produces more accurate abundance fraction estimation, thus better performance [5], [16], [19].

According to (2) the least squares error is equally weighted for all bands which are assumed to have their uniform effects on LSE. In general, this may not be necessarily true. To generalize this concept, we consider a weighted LSE approach to (2) by introducing a weighting matrix  $\mathbf{A}$  into (2) so that the LSE is weighted by  $\mathbf{A}$  via

$$(\mathbf{r} - \mathbf{M}\boldsymbol{\alpha})^T \mathbf{A} (\mathbf{r} - \mathbf{M}\boldsymbol{\alpha}). \quad (3)$$

Equation (3) is reduced to (2) if  $\mathbf{A} = \mathbf{I}$ , identity matrix. The key to success in using (3) is to find an appropriate weighting matrix  $\mathbf{A}$  that accounts for individual bands. As inspired by the three signal

Manuscript received October 13, 2004; revised September 9, 2005.

The authors are with the Remote Sensing Signal and Image Processing Laboratory, Department of Computer Science and Electrical Engineering, University of Maryland, Baltimore County, Baltimore, MD 21250 USA (e-mail: cchang@umbc.edu).

Digital Object Identifier 10.1109/TGRS.2005.861408

processing perspectives studied in [1] and [20] for LSMA, this paper investigates constrained LSMA with three different ways to select the weighting matrix  $\mathbf{A}$  for (3), which are also derived from the same three perspectives. One is based on the parameter estimation perspective that is derived from the well-known Mahalanobis distance [21] or Gaussian maximum-likelihood estimator (GMLE) [22]. If the weighting matrix  $\mathbf{A}$  in (3) is selected to be the inverse of the data sample covariance matrix  $\mathbf{K}$ ,  $\mathbf{K}^{-1}$ , (3) becomes the Mahalanobis distance (MD) or Gaussian maximum-likelihood estimator. The resulting constrained AC-LSMA is called MD-weighted AC-LSMA. As an alternative, if the weighting matrix  $\mathbf{A}$  in (3) is replaced with  $\mathbf{R}^{-1}$  (i.e., the inverse of data sample correlation matrix  $\mathbf{R}$ ), (3) is then reduced to a form of the linearly constrained minimum variance (LCMV) classifier [1], [23] which is referred to as LCMV-weighted AC-LSMA. Another selection of the weighting matrix is based on pattern classification perspective which is derived from Fisher's linear discriminant analysis (FLDA) [24]. It has been shown in [25] and [26] that with constraining Fisher's feature vectors to mutual orthogonal directions, maximizing Fisher's ratio is reduced to minimizing the within-class scatter matrix  $\mathbf{S}_W$ . As a result, selecting the  $\mathbf{S}_W^{-1}$  for the weighting matrix  $\mathbf{A}$  in (3) yields abundance-constrained Fisher's LSMA (AC-FLSMA) [23], [24], referred to as  $\mathbf{S}_W^{-1}$ -weighted AC-LSMA. A third way to select the weighting matrix is based on orthogonal subspace projection (OSP) [8] which is derived from signal detection perspective. It is shown in [1] and [20] that the undesired signature rejection matrix,  $P_U^\perp$ , used in the OSP can be approximated by  $\mathbf{R}^{-1}$  if the prior knowledge of the undesired signatures in  $\mathbf{U}$  is not available. Using this interpretation we can select  $P_U^\perp$  for the weighting matrix  $\mathbf{A}$  in (3), which results in OSP-weighted AC-LSMA. An interesting finding is that if the weighting matrix  $\mathbf{A}$  is selected by the signature subspace projection (SSP) matrix in [1] and [9] that is formed by the endmember matrix  $\mathbf{M}$  in (1) or (2), the resulting SSP-weighted AC-LSMA can be shown to be identical to the unweighted AC-LSMA in (2), in which case the  $\mathbf{A}$  becomes the identity matrix. This is due to the fact that both the SSP approach and LSMA are least squares-based methods. As a consequence, the weighted matrix specified by the SSP does not provide any additional advantage. Nevertheless, as will be demonstrated by experiments, all these three types of weighted AC-LSMA specified by appropriate selections for the weight matrix  $\mathbf{A}$  in (3) generally perform better than unweighted AC-LSMA described by (2).

This paper is organized as follows. Section II reviews the unweighted abundance-constrained LSMA. Section III presents three weighted LSE approaches to abundance-constrained LSMA. Section IV conducts computer simulations and real image experiments for performance analysis. Section V concludes some remarks.

## II. ABUNDANCE-CONSTRAINED LSMA

When unconstrained LSMA specified by (1) is considered, its unconstrained LSE solution to (2) is given by

$$\hat{\alpha}(\mathbf{r}) = (\mathbf{M}^T \mathbf{M})^{-1} \mathbf{M}^T \mathbf{r}. \quad (4)$$

Imposing the ASC and ANC on (2) results in three abundance-constrained LSE AC-LSMA problems of interest [1], [13], [16] as follows.

- 1) Abundance sum-to-one constrained LSMA problem

$$\min_{\alpha} \{(\mathbf{r} - \mathbf{M}\alpha)^T (\mathbf{r} - \mathbf{M}\alpha)\} \text{ subject to } \sum_{j=1}^p \alpha_j = 1. \quad (5)$$

- 2) Abundance nonnegativity-constrained LSMA problem

$$\min_{\alpha} \{(\mathbf{r} - \mathbf{M}\alpha)^T (\mathbf{r} - \mathbf{M}\alpha)\} \text{ subject to } \alpha \geq \mathbf{0}. \quad (6)$$

- 3) Abundance fully constrained LSMA problem

$$\min_{\alpha} \{(\mathbf{r} - \mathbf{M}\alpha)^T (\mathbf{r} - \mathbf{M}\alpha)\} \\ \text{subject to } \alpha \geq \mathbf{0} \text{ and } \sum_{j=1}^p \alpha_j = 1. \quad (7)$$

The solutions to the above LSE AC-LSMA described by (5)–(7) are well documented in [1], [13], and [16] and referred to as SCLS, NCLS, and FCLS, respectively, throughout this paper.

## III. WEIGHTED LEAST SQUARES AC-LSMA

It should be noted that the LSE specified by (2) does not include any weighting matrix to account for significance of each band, in which case the weighting matrix  $\mathbf{A}$  is chosen to be the identity matrix  $\mathbf{I}$  in (5)–(7). However, this is not necessarily an optimal way to impose the LSE since the LSE caused by every band is not necessarily equally significant. If a weighting matrix  $\mathbf{A}$  is included in (3) to account for the LSEs resulting from different bands (i.e., replace the  $\mathbf{I}$  in (2) with  $\mathbf{A}$ ), (2) becomes the  $\mathbf{A}$ -weighted LSE problem specified by (3) which is to find a solution that solves

$$\min_{\alpha} \{(\mathbf{r} - \mathbf{M}\alpha)^T \mathbf{A} (\mathbf{r} - \mathbf{M}\alpha)\}. \quad (8)$$

Suppose that  $\mathbf{A}$  is a positive-definite and symmetric matrix. We can use  $\mathbf{A}^{1/2}$ , the square-root form of  $\mathbf{A}$  to whiten the LSE in (8) as follows

$$\begin{aligned} & (\mathbf{r} - \mathbf{M}\alpha)^T (\mathbf{A}^{1/2})^T \mathbf{A}^{1/2} (\mathbf{r} - \mathbf{M}\alpha) \\ &= (\mathbf{A}^{1/2} \mathbf{r} - \mathbf{A}^{1/2} \mathbf{M}\alpha)^T (\mathbf{A}^{1/2} \mathbf{r} - \mathbf{A}^{1/2} \mathbf{M}\alpha). \end{aligned} \quad (9)$$

Using a linear transformation  $\xi_{\mathbf{A}}$  defined by

$$\hat{\mathbf{r}} = \xi_{\mathbf{A}}(\mathbf{r}) = \mathbf{A}^{1/2} \mathbf{r} \quad \hat{\mathbf{M}} = \xi_{\mathbf{A}}(\mathbf{M}) = \mathbf{A}^{1/2} \mathbf{M} \quad (10)$$

an  $\mathbf{A}$ -whitened LSE can be further simplified by  $\xi_{\mathbf{A}}$  and given by

$$\min_{\alpha} \{(\hat{\mathbf{r}} - \hat{\mathbf{M}}\alpha)^T (\hat{\mathbf{r}} - \hat{\mathbf{M}}\alpha)\} \quad (11)$$

which is reduced to minimization of (2) except that both the image pixel vector  $\mathbf{r}$  and the matrix  $\mathbf{M}$  have been whitened by the weighting matrix  $\mathbf{A}$  via the transformation  $\xi_{\mathbf{A}}$ . As a result, a new set of three types of  $\mathbf{A}$ -weighted AC-LSMA that are

similar to (5)–(7) can be also derived by replacing  $\mathbf{M}$  in (5)–(7) with  $\hat{\mathbf{M}}$  via  $\xi_{\mathbf{A}}$  in (10) and they are referred to as MD-weighted SCLS, MD-weighted NCLS, MD-weighted FCLS problems, respectively.

As shown in [1] and [20], the LSMA can be interpreted from three different signal processing perspectives, signal detection which results in the orthogonal subspace projection (OSP) approach, parameter estimation which results in Mahalanobis distance (MD) or Gaussian maximum-likelihood estimator (GMLE), and pattern classification which results in Fisher's linear discriminant analysis. Following the same treatment, these three signal processing perspectives can be also used to develop in parallel various versions of  $\mathbf{A}$ -weighted AC LSMA by appropriately selecting a weighted matrix  $\mathbf{A}$  in (3).

#### A. Weighting Matrix Derived From Parameter Estimation Perspective

Two ways to select the weighting matrix  $\mathbf{A}$  in (3) that accounts for spectral correlation used in the parameter estimation are the use of the covariance spectral matrix  $\mathbf{K}$  and the correlation spectral matrix  $\mathbf{R}$ .

1) *MD-Weighted AC-LSMA*: One of the well-known examples to weight mean squared error is Mahalanobis distance (MD), also known as GMLE which uses the data covariance matrix  $\mathbf{K}^{-1}$  as a weighting matrix. Substituting  $\mathbf{K}^{-1}$  for  $\mathbf{A}$  in (8) yields

$$\min_{\alpha} \{(\mathbf{r} - \mathbf{M}\alpha)^T \mathbf{K}^{-1} (\mathbf{r} - \mathbf{M}\alpha)\}. \quad (12)$$

Replacing the  $\mathbf{A}$  in (10) with  $\mathbf{K}^{-1}$  yields a new linear transformation  $\xi_{\mathbf{K}^{-1}}$  given by

$$\hat{\mathbf{r}} = \xi_{\mathbf{K}^{-1}}(\mathbf{r}) = \mathbf{K}^{-1/2} \mathbf{r} \quad \hat{\mathbf{M}} = \xi_{\mathbf{K}^{-1}}(\mathbf{M}) = \mathbf{K}^{-1/2} \mathbf{M}. \quad (13)$$

Then the resulting  $\mathbf{K}^{-1}$ -whitened LSE is found by

$$\min_{\alpha} \{(\hat{\mathbf{r}} - \hat{\mathbf{M}}\alpha)^T (\hat{\mathbf{r}} - \hat{\mathbf{M}}\alpha)\} \quad (14)$$

which is similar to (11). By virtue of (14), another new set of three types of  $\mathbf{A}$ -weighted AC-LSMA can be derived by replacing  $\mathbf{M}$  in (5)–(7) with  $\hat{\mathbf{M}}$  via  $\xi_{\mathbf{K}^{-1}}$  in (13) and they are referred to as MD-weighted SCLS, MD-weighted NCLS, MD-weighted FCLS problems, respectively.

2) *LCMV-Weighted AC-LSMA*: The LSE in (12) was derived from the MD or Gaussian maximum-likelihood estimation. If the data covariance matrix  $\mathbf{K}$  in (12) is replaced with the data correlation matrix  $\mathbf{R}$ , an LCMV-based abundance-constrained LSE problem can be derived by

$$\min_{\alpha} \{(\mathbf{r} - \mathbf{M}\alpha)^T \mathbf{R}^{-1} (\mathbf{r} - \mathbf{M}\alpha)\} \quad (15)$$

which uses the data correlation matrix  $\mathbf{R}$  as a weighting matrix. Using a linear transformation  $\xi_{\mathbf{R}^{-1}}$  similar to  $\xi_{\mathbf{K}^{-1}}$  defined in (13) by mapping  $\mathbf{r}$  and  $\mathbf{M}$  into

$$\bar{\mathbf{r}} = \xi_{\mathbf{R}^{-1}}(\mathbf{r}) = \mathbf{R}^{-1/2} \mathbf{r} \quad \bar{\mathbf{M}} = \xi_{\mathbf{R}^{-1}}(\mathbf{M}) = \mathbf{R}^{-1/2} \mathbf{M} \quad (16)$$

we can also obtain an  $\mathbf{R}^{-1}$ -whitened LSE problem given by

$$\min_{\alpha} \{(\bar{\mathbf{r}} - \bar{\mathbf{M}}\alpha)^T (\bar{\mathbf{r}} - \bar{\mathbf{M}}\alpha)\} \quad (17)$$

which is a correlation-based LSE problem. Three types of LCMV-weighted AC-LSMA can be derived by replacing  $\mathbf{M}$  in (5)–(7) with  $\hat{\mathbf{M}}$  via  $\xi_{\mathbf{R}^{-1}}$  in (16) and they are referred to as LCMV-weighted SCLS, LCMV-weighted NCLS, LCMV-weighted FCLS problems, respectively.

#### B. Weighting Matrix Derived From Fisher's Linear Discriminant Analysis Perspective

FLDA is one of the most widely used pattern classification techniques in pattern recognition [1], [24]. An application of the FLDA to hyperspectral image classification was also explored in [1], [25], and [26]. Its strength in pattern classification lies on the criterion used for optimality, which is called Fisher's ratio defined by the ratio of between-class scatter matrix to within-class scatter matrix. More specifically, assume that there are  $n$  training sample vectors given by  $\{\mathbf{r}_i\}_{i=1}^n$  for  $p$ -class classification,  $C_1, C_2, \dots, C_p$  with  $n_j$  being the number of training sample vectors in  $j$ th class  $C_j$ . Let  $\boldsymbol{\mu}$  be the global mean of the entire training sample vectors, denoted by  $\boldsymbol{\mu} = (1/n) \sum_{i=1}^n \mathbf{r}_i$  and  $\boldsymbol{\mu}_j$  be the mean of the training sample vectors in the  $j$ th class  $C_j$ , denoted by  $\boldsymbol{\mu}_j = (1/n_j) \sum_{\mathbf{r}_i \in C_j} \mathbf{r}_i$ . Now, we can define the within-class scatter matrix,  $\mathbf{S}_W$  and between-class scatter matrix  $\mathbf{S}_B$  as follows:

$$\mathbf{S}_W = \sum_{j=1}^p \mathbf{S}_j$$

where

$$\mathbf{S}_j = \sum_{\mathbf{r} \in C_j} (\mathbf{r} - \boldsymbol{\mu}_j)(\mathbf{r} - \boldsymbol{\mu}_j)^T \quad (18)$$

$$\mathbf{S}_B = \sum_{j=1}^p n_j (\boldsymbol{\mu}_j - \boldsymbol{\mu})(\boldsymbol{\mu}_j - \boldsymbol{\mu})^T. \quad (19)$$

Using (18) and (19), Fisher's ratio (also known as Rayleigh's quotient) is then defined by

$$\frac{\mathbf{x}^T \mathbf{S}_B \mathbf{x}}{\mathbf{x}^T \mathbf{S}_W \mathbf{x}} \text{ for any vector } \mathbf{x}. \quad (20)$$

The Fisher linear discriminant analysis is to find a set of feature vectors that maximize Fisher's ratio specified by (20). The number of feature vectors found by Fisher's ratio is determined by the number of classes,  $p$ , to be classified, which is  $p - 1$ .

It has been shown in [25] and [26] that a Fisher's ratio-based LSE problem, referred to as Fisher linear spectral mixture analysis (FLSMA), could be formulated as

$$\min_{\alpha} \{(\mathbf{r} - \mathbf{M}\alpha)^T \mathbf{S}_W^{-1} (\mathbf{r} - \mathbf{M}\alpha)\} \quad (21)$$

with  $\mathbf{S}_W^{-1}$  being used as a weighting matrix to replace the weighting matrix  $\mathbf{A}$  in (8). So, using a transformation  $\xi_{\mathbf{S}_W^{-1}}$  defined by

$$\tilde{\mathbf{r}} = \xi_{\mathbf{S}_W^{-1}}(\mathbf{r}) = \mathbf{S}_W^{-1/2} \mathbf{r} \quad \tilde{\mathbf{M}} = \xi_{\mathbf{S}_W^{-1}}(\mathbf{M}) = \mathbf{S}_W^{-1/2} \mathbf{M} \quad (22)$$

(21) can be whitened by  $\mathbf{S}_W^{-1}$  and becomes

$$\min_{\alpha} \{(\tilde{\mathbf{r}} - \tilde{\mathbf{M}}\alpha)^T (\tilde{\mathbf{r}} - \tilde{\mathbf{M}}\alpha)\}. \quad (23)$$

Therefore, three types of  $\mathbf{S}_W^{-1}$ -weighted AC-LSMA can be derived by replacing  $\mathbf{M}$  in (5)–(7) with  $\tilde{\mathbf{M}}$  via  $\xi_{\mathbf{S}_W^{-1}}$  in (22) and are referred to as  $\mathbf{S}_W^{-1}$ -weighted SCLS,  $\mathbf{S}_W^{-1}$ -weighted NCLS,  $\mathbf{S}_W^{-1}$ -weighted FCLS problems, respectively.

### C. Weighting Matrix Derived From Orthogonal Subspace Projection Perspective

As we have seen in Sections III-A and B, the weighting matrix  $\mathbf{A}$  was selected by sample spectral correlation matrices and Fisher's ratio which were resulting from the maximum-likelihood estimator and Fisher's linear discriminant analysis. In this section, we investigate the selection of the weighting matrix  $\mathbf{A}$  based on various OSP criteria.

1) *OSP-Weighted AC-LSMA*: According to the signal-decomposed interference-annihilated (SDIA) model in [27], the signal sources can be decomposed into desired signal sources which are assumed to be in the signature matrix  $\mathbf{M}$  and unwanted signal sources which are assumed to be interferers to the signal sources in the  $\tilde{\mathbf{M}}$ . If we let  $\mathbf{U}$  be the unwanted signature matrix made up of such interferers, we can project all image pixels onto the space  $\langle \mathbf{U} \rangle^\perp$  that is orthogonal to the space linearly spanned by the signal sources in  $\mathbf{U}$  and then perform the LSE problem specified by (2) in  $\langle \mathbf{U} \rangle^\perp$ . Inspired by this approach, the weighting matrix  $\mathbf{A}$  in (8) can be selected by the unwanted signature rejector,  $P_U^\perp$  defined in [28] by

$$P_U^\perp = \mathbf{I} - \mathbf{U}(\mathbf{U}^T\mathbf{U})^{-1}\mathbf{U}^T. \quad (24)$$

The resulting LSE problem from replacing  $\mathbf{A}$  in (8) with  $P_U^\perp$  in (24) is

$$\min_{\boldsymbol{\alpha}} \{(\mathbf{r} - \mathbf{M}\boldsymbol{\alpha})^T P_U^\perp (\mathbf{r} - \mathbf{M}\boldsymbol{\alpha})\}. \quad (25)$$

Since  $P_U^\perp$  is idempotent,  $P_U^\perp = (P_U^\perp)^2$  and  $(P_U^\perp)^T = P_U^\perp$ . This implies that

$$\begin{aligned} (\mathbf{r} - \mathbf{M}\boldsymbol{\alpha})^T P_U^\perp (\mathbf{r} - \mathbf{M}\boldsymbol{\alpha}) &= (\mathbf{r} - \mathbf{M}\boldsymbol{\alpha})^T (P_U^\perp)^T P_U^\perp (\mathbf{r} - \mathbf{M}\boldsymbol{\alpha}) \\ &= (P_U^\perp \mathbf{r} - P_U^\perp \mathbf{M}\boldsymbol{\alpha})^T (P_U^\perp \mathbf{r} - P_U^\perp \mathbf{M}\boldsymbol{\alpha}). \end{aligned} \quad (26)$$

Using a linear transformation  $\xi_{P_U^\perp}$  defined by mapping  $\mathbf{r}$  and  $\mathbf{M}$  into

$$\tilde{\mathbf{r}} = \xi_{P_U^\perp}(\mathbf{r}) = P_U^\perp \mathbf{r} \quad \tilde{\mathbf{M}} = \xi_{P_U^\perp}(\mathbf{M}) = P_U^\perp \mathbf{M} \quad (27)$$

we can also obtain a similar form to (11) given by

$$\min_{\boldsymbol{\alpha}} \{(\tilde{\mathbf{r}} - \tilde{\mathbf{M}}\boldsymbol{\alpha})^T (\tilde{\mathbf{r}} - \tilde{\mathbf{M}}\boldsymbol{\alpha})\} \quad (28)$$

which is referred to as OSP-weighted abundance-constrained LSE problem. Consequently, three types of OSP-weighted AC LSMA can be derived by replacing  $\mathbf{M}$  in (5)–(7) with  $\tilde{\mathbf{M}}$  via  $\xi_{P_U^\perp}$  in (27) and they are referred to as OSP-weighted SCLS, OSP-weighted NCLS, OSP-weighted FCLS problems, respectively. A key to success in the OSP-weighted ACLSMA is to find the unknown signal sources used in the matrix  $\mathbf{U}$  in an unsupervised manner. The one of particular interest is called automatic target detection and classification algorithm (ATDCA) that was developed in [29] and can be used for this purpose.

2) *SSP-Weighted AC-LSMA*: As an alternative to (28), we can also formulate an LSE problem based on performing abundance estimation in the space that is linearly spanned by the signal sources in the signature matrix  $\mathbf{M}$  exclusively. Such an LSE problem resulting from replacing  $P_U^\perp$  in (24) with a signature subspace projector,  $P_M$  defined in [1], [9], [28], and [30] by

$$P_M = \mathbf{M}(\mathbf{M}^T\mathbf{M})^{-1}\mathbf{M}^T \quad (29)$$

is referred to as SSP-weighted AC-LSMA which is to find the solution to the following optimization problem:

$$\min_{\boldsymbol{\alpha}} \{(\mathbf{r} - \mathbf{M}\boldsymbol{\alpha})^T P_M (\mathbf{r} - \mathbf{M}\boldsymbol{\alpha})\}. \quad (30)$$

Once again,  $P_M$  is idempotent,  $(P_M)^2 = P_M$  and  $(P_M)^T = P_M$ . Using a linear transformation  $\xi_{P_M}$  defined by mapping  $\mathbf{r}$  and  $\mathbf{M}$  into

$$\tilde{\mathbf{r}} = \xi_{P_M}(\mathbf{r}) = P_M \mathbf{r} \quad \tilde{\mathbf{M}} = \xi_{P_M}(\mathbf{M}) = P_M \mathbf{M} = \mathbf{M} \quad (31)$$

(30) becomes

$$\min_{\boldsymbol{\alpha}} \{(\tilde{\mathbf{r}} - \mathbf{M}\boldsymbol{\alpha})^T (\tilde{\mathbf{r}} - \mathbf{M}\boldsymbol{\alpha})\}. \quad (32)$$

Interestingly, the solution to (32) is

$$\begin{aligned} \hat{\boldsymbol{\alpha}}(\tilde{\mathbf{r}}) &= (\mathbf{M}^T\mathbf{M})^{-1}\mathbf{M}^T\tilde{\mathbf{r}} = (\mathbf{M}^T\mathbf{M})^{-1}\mathbf{M}^T P_M \mathbf{r} \\ &= (\mathbf{M}^T\mathbf{M})^{-1}\mathbf{M}^T\mathbf{M}(\mathbf{M}^T\mathbf{M})^{-1}\mathbf{M}^T \mathbf{r} \\ &= (\mathbf{M}^T\mathbf{M})^{-1}\mathbf{M}^T \mathbf{r} = \hat{\boldsymbol{\alpha}}(\mathbf{r}) \end{aligned} \quad (33)$$

which is identical to the unconstrained least squares LSMA solution given by (4). As a result, the three types of SSP-weighted AC-LSMA obtained by the linear transformation  $\xi_{P_M}$  in (31) turn out to be the same unweighted ASC-LSMA. ANC-LSMA and AFC-LSMA described by (5)–(7). This is because the weighted matrix specified by the SSP does not provide any additional advantage as shown by (31) and (33) due to the fact that  $P_M \mathbf{M} = \mathbf{M}$ .

## IV. EXPERIMENTS

This section conducts two sets of experiments, computer simulations and real image experiments to demonstrate the utility of various weighted least squares error approaches to AC-LSMA. All the experiments were based on a Hyperspectral Digital Image Collection Experiment (HYDICE) image scene shown in Fig. 1(a), which has a size of  $64 \times 64$  pixel vectors with 15 panels in the scene and the ground truth map in Fig. 1(b) [1]. It was acquired by 210 spectral bands with a spectral coverage from 0.4–2.5  $\mu\text{m}$ . Low signal/high noise bands: bands 1–3 and bands 202–210; and water vapor absorption bands: bands 101–112 and bands 137–153 were removed. So, a total of 169 bands were used. The spatial resolution is 1.56 m and spectral resolution is 10 nm. Within the scene in Fig. 1(a) there is a large grass field background, and a forest on the left edge. Each element in this matrix is a square panel.

For each row  $i = 1, 2, \dots, 5$ , the three panels were painted by the same material but have three different sizes. For each column  $j = 1, 2, 3$ , the five panels have the same size but were painted

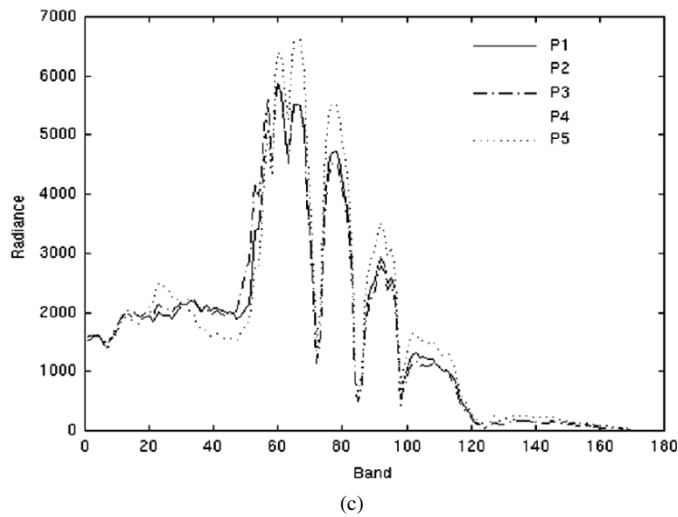
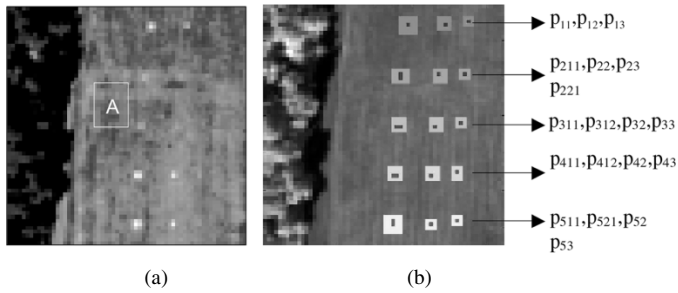


Fig. 1. (a) HYDICE panel scene which contains 15 panels. (b) Ground truth map of spatial locations of the 15 panels. (c) Spectral signatures of  $P_1$ ,  $P_2$ ,  $P_3$ ,  $P_4$ , and  $P_5$ .

by five different materials. It should be noted that the panels in rows 2 and 3 are made by the same material with different paints, so did the panels in rows 4 and 5. Nevertheless, they were still considered as different materials. The sizes of the panels in the first, second and third columns are  $3\text{ m} \times 3\text{ m}$ ,  $2\text{ m} \times 2\text{ m}$ , and  $1\text{ m} \times 1\text{ m}$ , respectively. So, the 15 panels have five different materials and three different sizes. Fig. 1(b) shows the precise spatial locations of these 15 panels where red (R) pixels are the panel center pixels shown as black pixels in grayscale images and the pixels in yellow (Y) are panel pixels mixed with background and shown as white pixels in grayscale images. The 1.56-m spatial resolution of the image scene suggests that the panels in the second and third columns, denoted by  $P_{12}$ ,  $P_{13}$ ,  $P_{22}$ ,  $P_{23}$ ,  $P_{32}$ ,  $P_{33}$ ,  $P_{42}$ ,  $P_{43}$ ,  $P_{52}$ ,  $P_{53}$  in Fig. 1(b) are one pixel in size. Additionally, except the panel in the first row and first column, denoted by  $p_{11}$  which also has size of one pixel, all other panels located in the first column are two-pixel panels which are the panel in the second row with two pixels lined up vertically, denoted by  $p_{211}$  and  $p_{221}$ , the panel in the third row with two pixels lined up horizontally, denoted by  $p_{311}$  and  $p_{312}$ , the panel in the fourth row with two pixels also lined up horizontally, denoted by  $p_{411}$  and  $p_{412}$ , and the panel in the fifth row with two pixels lined up vertically, denoted by  $p_{511}$  and  $p_{521}$ . Since the size of the panels in the third column is  $1\text{ m} \times 1\text{ m}$ , they cannot be seen visually from Fig. 1(a) due to the fact that its size is less than the 1.56-m pixel resolution. Fig. 1(c) plots the five panel spectral signatures  $p_i$  for  $i = 1, 2, \dots, 5$  obtained by averaging R pixels in the  $3\text{ m} \times 3\text{ m}$  and  $2\text{ m} \times 2\text{ m}$

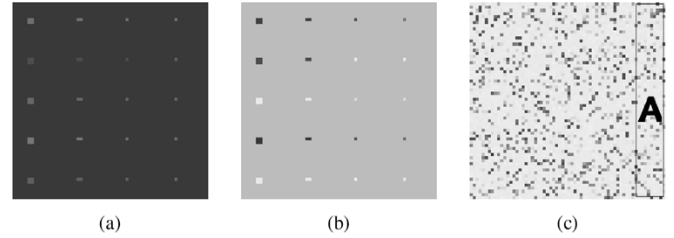


Fig. 2. Twenty-panel synthetic image. (a) Twenty simulated panels. (b) Panels with background. (c) Image with noise.

panels in row  $i$  in Fig. 1(b). It should be noted the R pixels in the  $1\text{ m} \times 1\text{ m}$  panels are not included because they are not pure pixels due to that fact that the spatial resolution of the R pixels in the  $1\text{ m} \times 1\text{ m}$  panels is 1 m smaller than the spatial resolution (ground sampling distance), 1.56 m, in which case the size of a  $1\text{ m} \times 1\text{ m}$  panel is  $1/(1.56)^2 = 0.41/\text{pixel}$  and can be considered as a subpixel panel. These panel signatures along with the R pixels in the  $3\text{ m} \times 3\text{ m}$  and  $2\text{ m} \times 2\text{ m}$  panels were used as required prior target knowledge for the following comparative studies.

#### A. Computer Simulations

In this section, a synthetic image similar to the real scene in Fig. 1(a) was simulated. It has size of  $64 \times 64$  pixel vectors and 20 panels with various sizes arranged in a  $5 \times 4$  matrix and located at the center of the scene shown in Fig. 2(a).

The five panel signatures in Fig. 1(c) were used to simulate these 20 panels. For row  $i$ , the panel signature  $p_i$  was used to simulate four panels with a  $2 \times 2$ -pixel panel,  $\{P_{1,11}^i, P_{1,12}^i, P_{1,21}^i, P_{1,22}^i\}$  in the first column, a  $1 \times 2$ -pixel panel,  $\{P_{2,11}^i, P_{2,12}^i\}$  in the second column, a one-pixel panel,  $p_{3,1}^i$  in the third column and a one-pixel panel,  $p_{4,1}^i$  in the fourth column, respectively. While the pixels in all the  $2 \times 2$ -pixel panels and the  $1 \times 2$ -pixel panels are pure pixels simulated by 100% panel signature  $p_i$ , the panels,  $p_{3,1}^i$  and  $p_{4,1}^i$  are subpixel panels simulated by  $(50\%p_i, 50\%b_A)$  and  $(25\%p_i, 75\%b_A)$  where the background signature,  $b_A$  was a grass signature obtained by averaging all the pixels in the area A marked in Fig. 2(c). Fig. 2(b) is a synthetic image simulated by implanting the 20 panels in Fig. 2(a) in the grass signature  $b_A$ -generated image background in Fig. 2(c). Fig. 2(c) was obtained by adding a Gaussian noise to the synthetic image in Fig. 2(b) with signal-to-noise ratio 20:1 defined in [8]. This synthetic image was particularly simulated to mimic the image scene in Fig. 1(a) for comparative analysis. Since full constraints, i.e., ASC+ANC on abundance fractions are of major interest in this paper, the algorithms to be evaluated for comparative analysis were weighted fully abundance constrained LSMA which are MD-weighted AC-LSMA, LCMV-weighted AC-LSMA,  $S_W^{-1}$ -weighted AC-LSMA, and OSP-weighted AC-LSMA plus the FCLS which is the unweighted AC-LSMA (i.e.,  $A = I$ , unweighting AC-LSMA) and also turns out to be the SSP-weighted AC-LSMA (i.e.,  $A^{-1} = P_M$ , unweighting AC-LSMA).

*Example 1 (With Complete Knowledge of Panel Signatures and Background Signature):* This example assumes that the complete knowledge of the five panel signatures in Fig. 1(c)

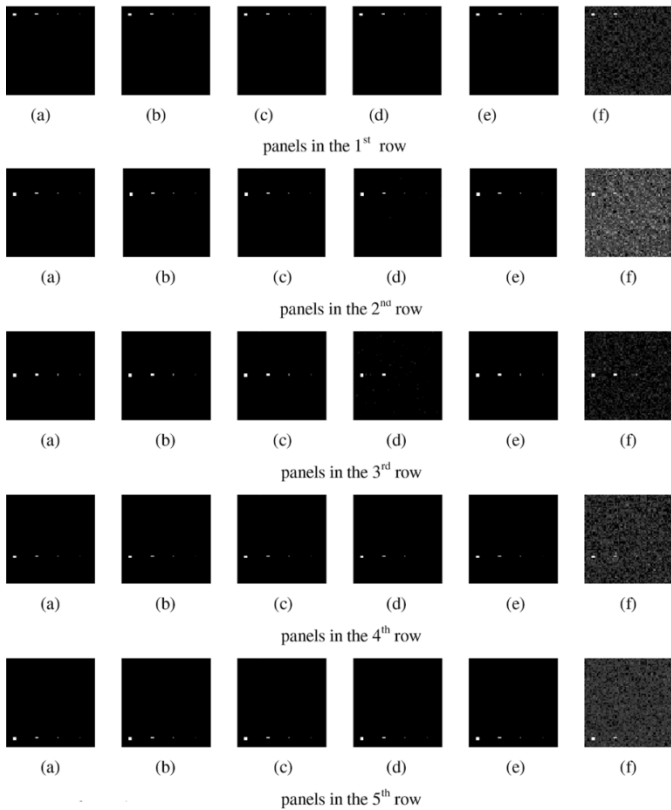


Fig. 3. Abundance fraction results of 20 panels estimated by the supervised five AC-LSMA methods and unconstrained LSOSP.

and the background signature  $\mathbf{b}_A$  was given *a priori*. Fig. 3 shows the abundance fractions of the 20 panels in Fig. 2(c) estimated by the six methods, (a) MD-weighted AC-LSMA, (b) LCMV-weighted AC-LSMA, (c)  $\mathbf{S}_W^{-1}$ -weighted AC-LSMA, (d) OSP-weighted AC-LSMA, (e) FCLS, and (f) unconstrained LSOSP, respectively, with additional results produced by the unconstrained LSOSP [30] included in Fig. 3 for comparison.

As shown in Fig. 3, all the weighted AL-LSMA methods produced very comparable results and performed significantly better than did the unconstrained LSOSP. It should be noted that the  $\mathbf{S}_W^{-1}$ -weighted AC-LSMA requires a training set to implement. For our experiments, the training samples were selected and consisted of the pixels in the  $2 \times 2$ -pixel panels in the first column of five rows in Fig. 2(a) and all background pixels in area A marked in Fig. 2(c). Also, when the OSP-weighted AC-LSMA was implemented, the threshold chosen empirically for the spectral angle mapper (SAM) to find interferers was set to 0.03 which resulted in 18 interferers. Fig. 4 graphically plots the abundance fractions of the 20 panels obtained for images in Fig. 3 for quantification analysis where the  $\mathbf{S}_W^{-1}$ -weighted AC-LSMA labeled by (c) was the best in producing accurate abundance fractions in most of the 20 panels. This was due to the fact that the  $\mathbf{S}_W^{-1}$ -weighted AC-LSMA used training samples to perform classification based on Fisher's ratio.

According to Fig. 4, both the MD-weighted AC-LSMA and LCMV-weighted AC-LSMA labeled by (a) and (b) performed very similarly. Surprisingly, the OSP-weighted AL-LSMA labeled by (d) did not perform as well as did the MD-weighted AC-LSMA and LCMV-weighted AC-LSMA. On the other

hand, the FCLS labeled by (e) seemed to perform very well and slightly better than the MD-weighted AC-LSMA and LCMV-weighted AC-LSMA in quantification of full panel pixels, but not for subpixel panels.

1) *Example 2 (With No Prior Knowledge About Panel Signatures and Background Signature)*: Unlike Example 1 no prior knowledge about the synthetic image in Fig. 2(c) was assumed. In particular, there was no knowledge about how many signatures that would represent the image scene. In this case, we ought to find a set of these signatures directly from the data in an unsupervised manner. First of all, we need to determine the number of signatures required to be generated for the scene. Recently, Chang and Du developed a concept, referred to as virtual dimensionality (VD) in [1] and [31] which provided a good estimate of the number of spectrally distinct signatures,  $p$  in hyperspectral image data where two proposed approaches, called Harsanyi–Farrand–Chang (HFC) method and noise-whitened HFC (NWHFC) method were used for this example to determine the  $p$ . Table I tabulates the VD estimated by the HFC and NWHFC methods in accordance with various false alarm probabilities indicated by  $P_F$ . According to Table I, a good estimate for the  $p$  was set to 6.

In order to produce a set of six desired signatures for the synthetic scene, the N-finder algorithm (N-FINDR) developed by Winter in [32] was used to find, six endmembers,  $\{\mathbf{e}_j\}_{j=1}^6$  shown in Fig. 5 that include five panel pixels specified by all the five different panel signatures,  $\{\mathbf{p}_i\}_{i=1}^5$  and one background pixel.

The spectral signatures of these six pixels were then used to form the desired signature matrix  $\mathbf{M}$ . Additionally, according to [27] the performance can be improved by eliminating interference prior to classification. In this case, the automatic target generation process (ATGP) developed for the automatic target detection and classification algorithm (ATDCA) in [1] and [29] was applied to find all potential interferers. The ATGP was terminated when a warning sign of matrix singularity occurred. Since some of the ATGP-generated target pixels may also happen to be very similar or identical to the N-FINDR-generated endmembers, these ATGP-generated target pixels could not be considered as interferers. So, when the OSP-weighted AC-LSMA was implemented, the unwanted signature matrix  $\mathbf{U}$  would be made up of all the ATGP-generated target pixels by excluding those that also happened to be N-FINDR generated endmembers. In this case, the SAM was set to 0.04 which was used to determine if an ATGP-target pixel was also an endmember. As a result, 22 interferers were found for OSP annihilation. On the other hand, when the  $\mathbf{S}_W^{-1}$ -weighted AC-LSMA was implemented, a set of training samples was required. In this case, the SAM was empirically set to 0.04 to find pixels that were similar to each of the six endmembers,  $\{\mathbf{e}_j\}_{j=1}^6$  to form a set of training data for each of the  $p$  classes,  $\{C_j\}_{j=1}^6$ . Then the means of each of the  $p$  classes were further calculated,  $\{\boldsymbol{\mu}_j\}_{j=1}^6$  to form the desired signature matrix  $\mathbf{M}$ . With the knowledge provided by the  $\mathbf{M}$  and  $\{C_j\}_{j=1}^6$ , the six methods, MD-weighted AC-LSMA, LCMV-weighted AC-LSMA,  $\mathbf{S}_W^{-1}$ -weighted AC-LSMA, OSP-weighted AC-LSMA, FCLS, and unconstrained LSOSP labeled by (a)–(f) were implemented for comparison. Fig. 6 shows their corresponding abundance

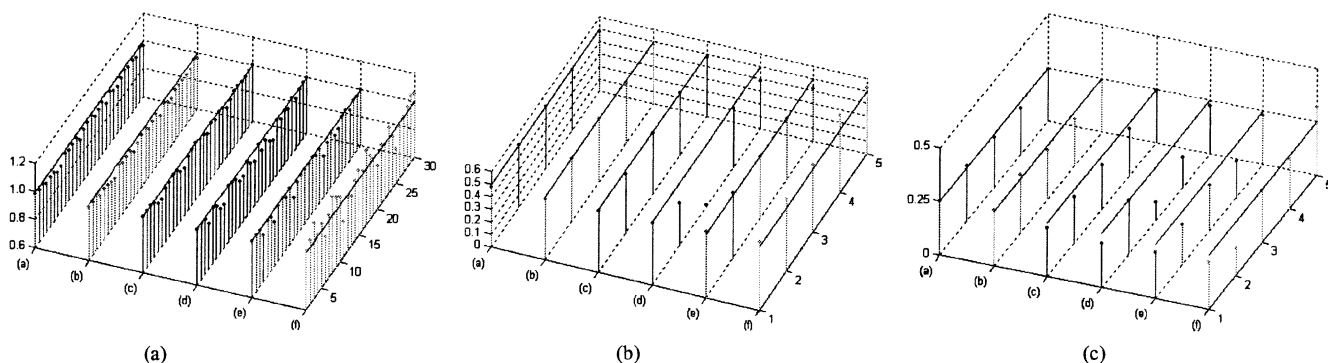


Fig. 4. Graphical representation of abundance fractions of panel pixels in Fig. 2(a) for visual assessment. (a) Thirty pure panel pixels in first and second columns. (b) Fifty percent subpixel panels in third column. (c) Twenty-five percent subpixel panels in fourth column.

TABLE I  
VD ESTIMATED BY THE HFC AND NWHFC METHODS WITH  
VARIOUS FALSE ALARM PROBABILITIES  $P_F$

	$P_F = 10^{-1}$	$P_F = 10^{-2}$	$P_F = 10^{-3}$	$P_F = 10^{-4}$
HFC	15	7	5	4
NWHFC	6	6	6	6

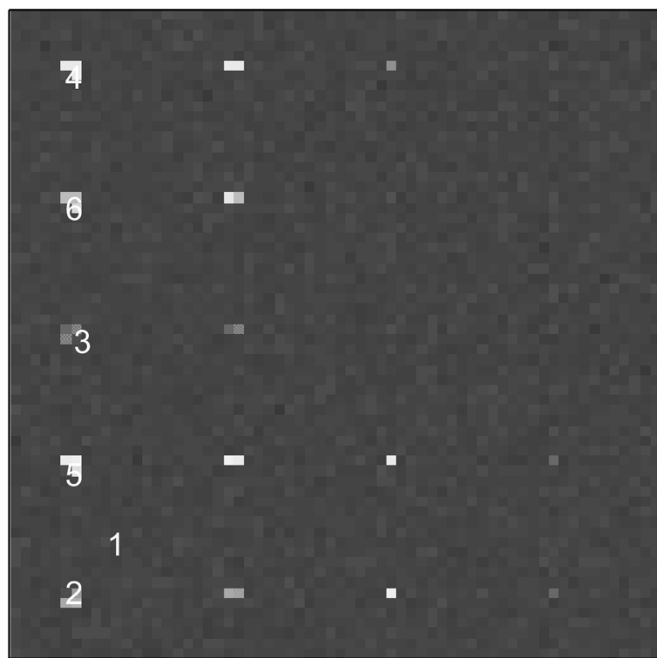


Fig. 5. Six endmembers produced by the N-FINDR.

fraction results of the 20 panels in Fig. 2(c) with full abundance constraints (i.e., ASC + ANC) respectively where the  $S_W^{-1}$ -weighted AC-LSMA clearly outperformed all other five methods and the unconstrained LSOSP was the worst.

Fig. 7 graphically plots the abundance fractions of the 20 panels obtained by the six methods (a)–(f) in Fig. 6 for quantification analysis where the  $S_W^{-1}$ -weighted AC-LSMA labeled by (c) was the only one produced most accurate abundance fractions of all 20 panels and performed very comparably to its supervised counterpart in Example 1. Unfortunately, it was not the case for all other five methods specified by (a)–(b) and (d)–(f) which apparently could not compete against their supervised counterparts in Example 1.

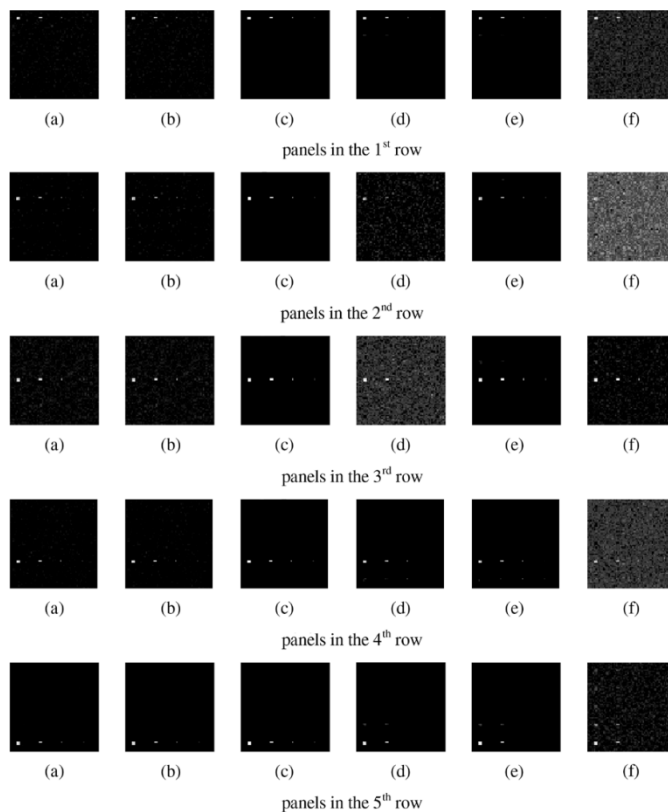


Fig. 6. Abundance fraction results of 20 panels estimated by unsupervised five AC-LSMA methods and unconstrained LSOSP.

### B. Real Image Experiments

In this section, the 15-panel HYDICE image scene in Fig. 1 was used for experiments. One major difference between the real HYDICE image scene in Fig. 1 and the simulated synthetic image in Fig. 2(c) is that very little knowledge of the image background in Fig. 1 was known compared to the image background in Fig. 2(b) which was simulated by complete knowledge. As we may expect, an AC-LSMA classifier may not perform as well as it did for the synthetic image if the image background in Fig. 1 is not well characterized. In order to demonstrate this fact, two scenarios were used to characterize the image background as follows. Additionally, we also assumed that the knowledge of the nine R pixels in the  $3 \times 3$  m and five R pixels in  $2 \times 2$  m panels in Fig. 1(b) was available

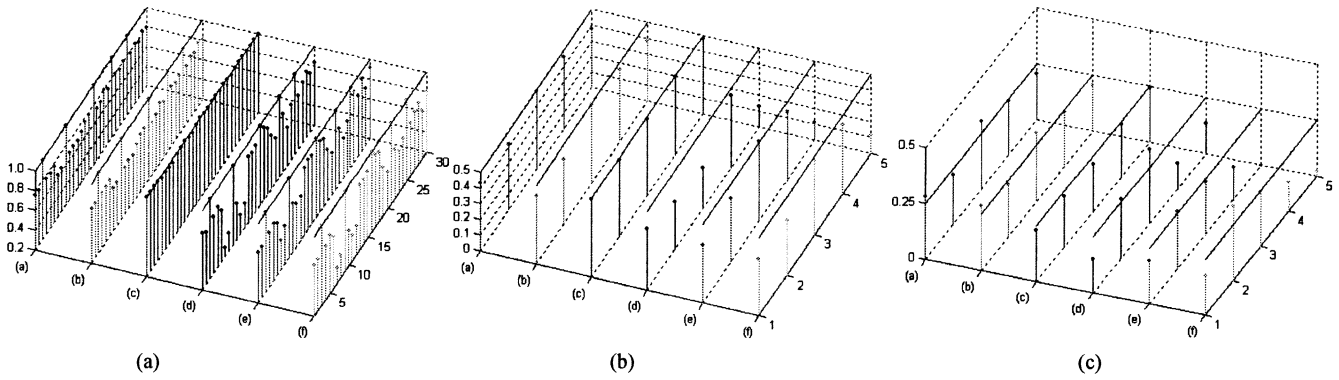


Fig. 7. Graphical representation of abundance fractions of panel pixels in Fig. 2(a) for visual assessment. (a) Thirty pure panel pixels in first and second columns. (b) Fifty percent subpixel panels in third column. (c) Twenty-five percent subpixel panels in fourth column.

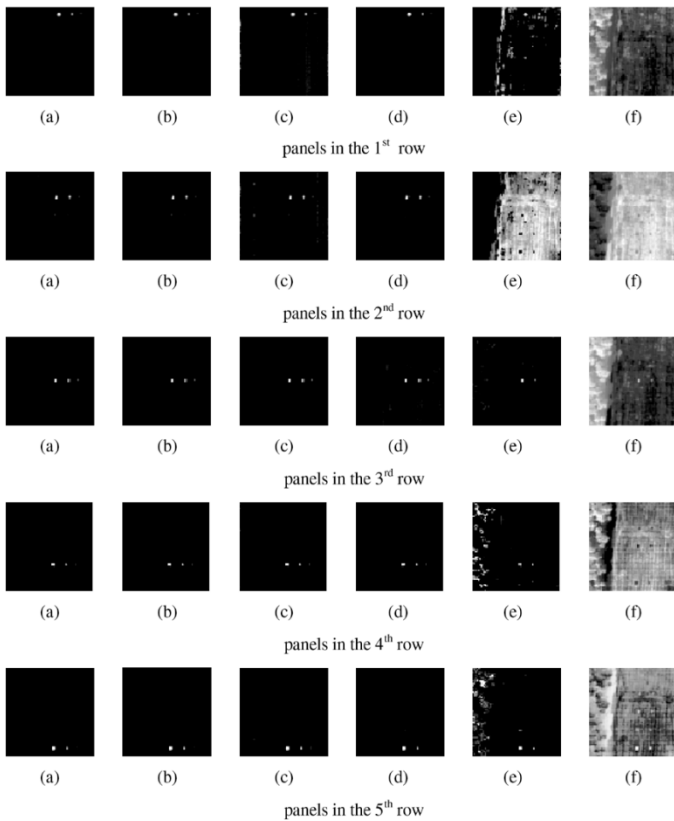


Fig. 8. Fifteen-panel abundance fraction results of the supervised five AC-LSMA methods and unconstrained LSOSP.

*a priori*. So, the panel signatures in Fig. 1(c) and 14 R pixels in both the 3 m × 3 m and 2 m × 2 m panels were considered to be prior knowledge.

By viewing the scene in Fig. 1(a), a large portion of the image background is made up of 1/4 of a forest on the left and 3/4 of a large grass field. Using this supervised knowledge, we conducted two experiments to represent the image background. One is to use the area A to characterize the image background. In this case, a single background signature  $\mathbf{b}_A$  was used for experiments, and the training samples used for  $\mathbf{S}_W^{-1}$ -weighted AC-LSMA were all the pixels in the area A for one background class as we did in Example 1. Another scenario was to use ATGP to produce necessary background knowledge in an unsupervised manner.

*Example 3 (Scenario 1: Single Background Signature):* Like Example 1, the signature matrix  $\mathbf{M}$  used for experiments was formed by  $\mathbf{M} = [\mathbf{p}_1 \mathbf{p}_2 \mathbf{p}_3 \mathbf{p}_4 \mathbf{p}_5 \mathbf{b}_A]$ . The 14 R pixels in both the 3 m × 3 m and 2 m × 2 m panels and pixels in the area A provided training samples for the  $\mathbf{S}_W^{-1}$ -weighted AC-LSMA. The six methods labeled by the five AC-LSMA methods, MD-weighted AC-LSMA, LCMV-weighted AC-LSMA,  $\mathbf{S}_W^{-1}$ -weighted AC-LSMA, OSP-weighted AC-LSMA, FCLS, and unconstrained LSOSP were evaluated for comparative analysis. Fig. 8 shows their respective abundance fraction results of the 15 panels in Fig. 1 with full abundance constraints (i.e., ASC+ANC), respectively. By visual inspection, once again, the unconstrained LSOSP was the worst. The MD-weighted AC-LSMA and LCMV-weighted AC-LSMA performed slightly better than  $\mathbf{S}_W^{-1}$ -weighted AC-LSMA and also seemed among the best.

For visual assessment, Fig. 9 further graphically plots the abundance fractions of the 14 pure R panel pixels (i.e.,  $P_{11}, P_{12}, P_{211}, P_{221}, P_{22}, P_{311}, P_{312}, P_{32}, P_{411}, P_{412}, P_{42}, P_{511}, P_{521}, P_{52}$ ) in Fig. 9(a) and abundance fractions of the five R panel subpixels (i.e.,  $P_{13}, P_{23}, P_{33}, P_{43}, P_{53}$ ) in Fig. 9(b) that were obtained by the six method labeled by (a)–(f) in Fig. 6. The quantification results show that the  $\mathbf{S}_W^{-1}$ -weighted AC-LSMA specified by (c) was the best in the sense that it produced the most accurate abundance fractions of the 19 panel pixels. Fig. 9 demonstrated that visual inspection of Fig. 8 may not provide reliable quantification estimates of abundance fractions.

*Example 4 (Scenario 2: Unsupervised Background Knowledge):* As demonstrated in Example 3, due to the fact that a single background signature could not completely characterize the image background, the AC-LSMA performance was not so good as it did for the synthetic image in Example 1. In order to improve its performance, we need to find an appropriate set of background pixels that can well represent the image background. According to [31], the number of spectrally distinct signatures in the scene in Fig. 1(a) was estimated by the VD as 18 via NWHFC. This implies that we need at least 13 distinct signatures to characterize the image background in addition to the five panel signatures in Fig. 1(c). In this case, the N-FINDR algorithm was applied to find the 18 endmembers,  $\{\mathbf{e}_j\}_{j=1}^{18}$  shown in Fig. 10 to form the desired signature matrix  $\mathbf{M}$  where the found pixels labeled by numbers 3, 5, 9, 15, and 17 in Fig. 7 represented five panel signatures in five different rows in Fig. 1.

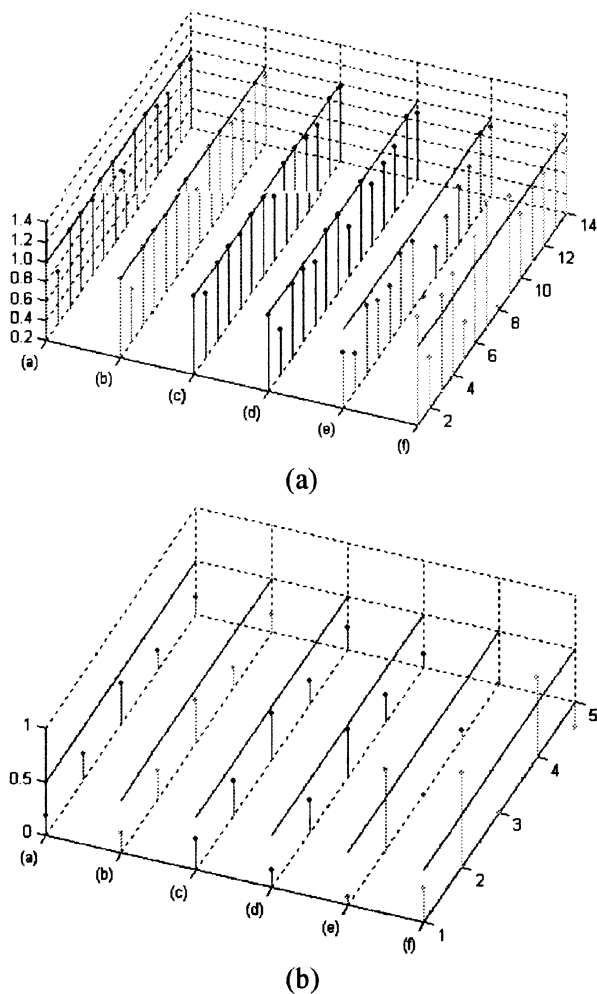


Fig. 9. Graphical representation of abundance fractions of 19 R panel pixels in Fig. 1(b) for visual assessment. (a) Fourteen R pure panel pixels in first and second columns. (b) Five R subpixel panels in third column.

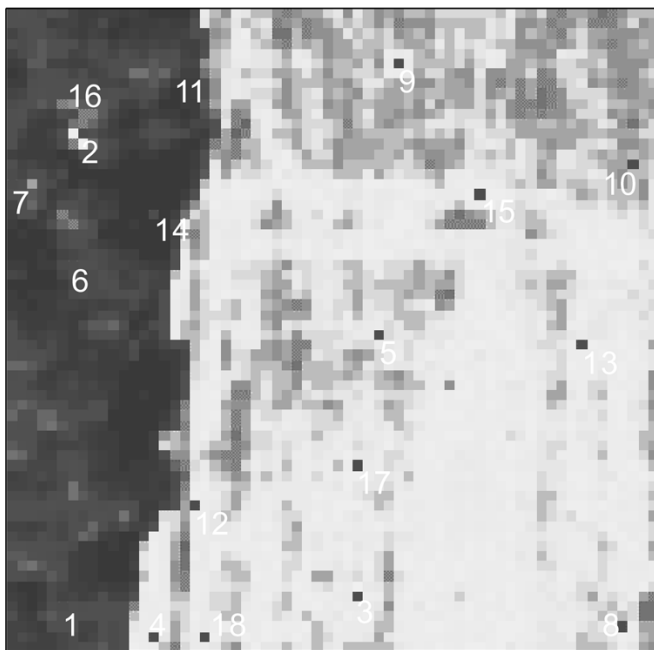


Fig. 10. Eighteen endmembers produced by the N-FINDR.

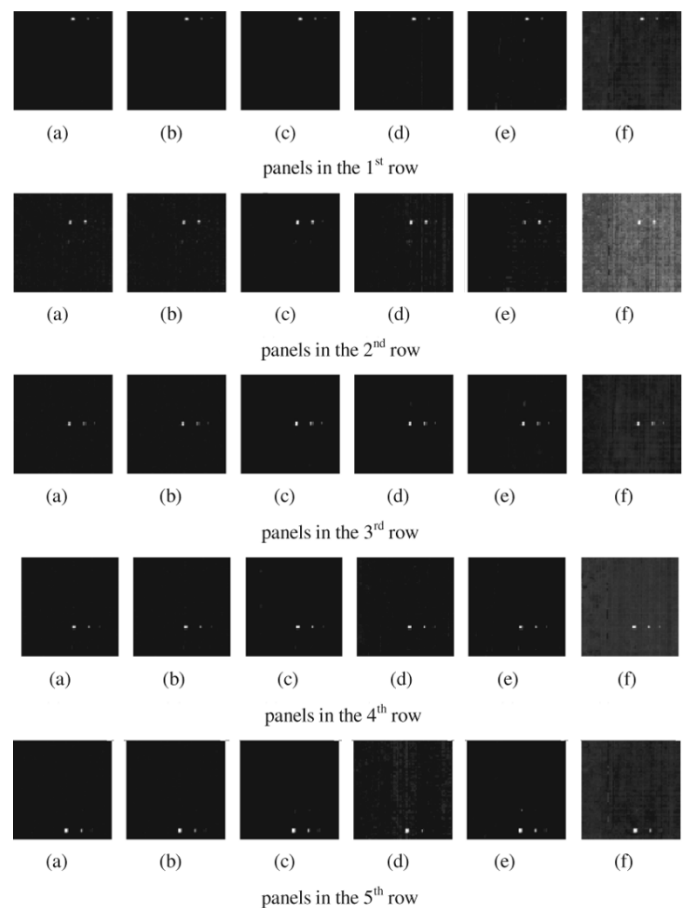


Fig. 11. Unsupervised 15-panel abundance fraction results of five AC-LSMA methods and unconstrained LSOSP.

In analogy with Example 2, the ATGP was implemented to find potential interferers, and the ATGP was implemented until a warning sign of matrix singularity occurred. In our experiments, there were 169 target pixels. Since some of such ATGP-generated target pixels may also happen to be very similar or identical to the 18 endmembers generated by the N-FINDR, these ATGP-generated target pixels could not be considered as interferers. So, when the OSP-weighted AC-LSMA was implemented, the unwanted signature matrix  $U$  would be made up of all the ATGP-generated target pixels except those that also happened to be N-FINDR-generated endmembers. In this case, the SAM was set to 0.06 to determine if an ATGP target pixel is also an endmember. On the other hand, when the  $S_W^{-1}$ -weighted AC-LSMA was implemented, a set of training samples was required. In this case, the SAM was empirically set to 0.025 to find pixels that were similar to each of the 18 endmembers,  $\{e_j\}_{j=1}^{18}$  to form a set of training data for each of the 18 classes,  $\{C_j\}_{j=1}^{18}$  where the total number of found training samples was 375. Then the mean of training samples in each of the 18 classes were further calculated,  $\{\mu_j\}_{j=1}^{18}$  to form the desired signature matrix  $M$ . Six methods, AC-LSMA methods, MD-weighted AC-LSMA, LCMV-weighted AC-LSMA,  $S_W^{-1}$ -weighted AC-LSMA, OSP-weighted AC-LSMA, FCLS, and unconstrained LSOSP labeled by (a)–(f) were evaluated for comparative analysis.

Fig. 11 shows their respective abundance fraction results of the 15 panels in Fig. 1 with full abundance constraints (i.e.,

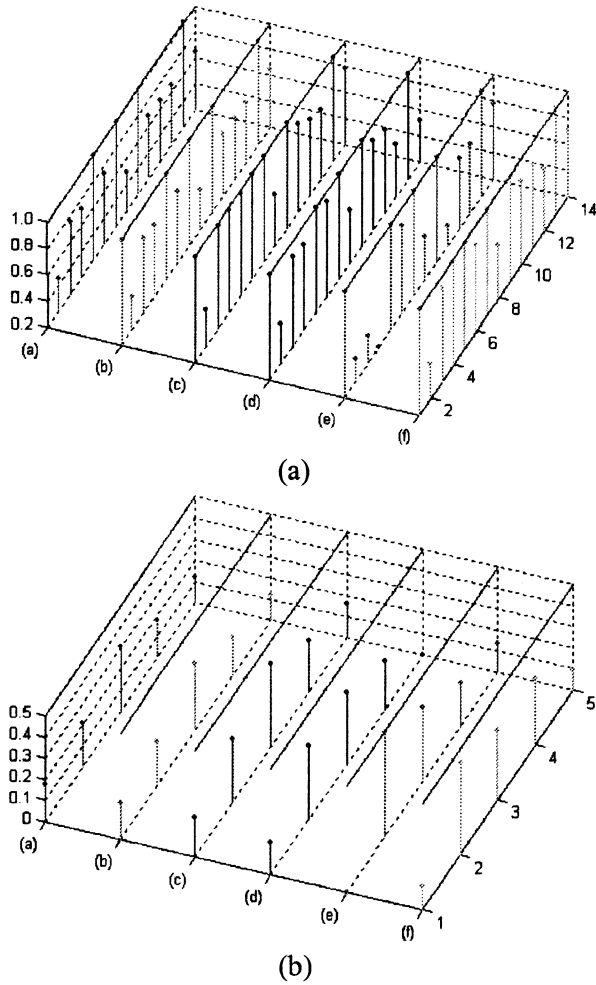


Fig. 12. Graphical representation of abundance fractions of 19 R panel pixels in Fig. 1(b) for visual assessment. (a) Fourteen R pure panel pixels in first and second columns. (b) Five R panel subpixels in third column.

ASC+ANC) where the  $\mathbf{S}_W^{-1}$ -weighted AC-LSMA was the best compared to the unconstrained LSOSP which was the worst.

Unlike Example 3, which only used one background signature, the use of additional 12 background signatures to find training samples made a significant difference for the  $\mathbf{S}_W^{-1}$ -weighted AC-LSMA. As shown in Fig. 11, the  $\mathbf{S}_W^{-1}$ -weighted AC-LSMA labeled by (c) clearly outperformed all other five AC-LSMA methods. Interestingly, the FCLS seemed to perform well in detection of 19 R panel pixels visually shown in Fig. 11 at the expense of many falsely alarmed pixels. However, their quantitative results plotted in Fig. 12 show otherwise where Fig. 12(a) and (b) plots quantified abundance fractions of 14 R pure panel pixels and five R panel subpixels in Fig. 11, respectively, where the MD-weighted AC-LSMA and LCMV-weighted AC-LSMA labeled by (a)–(b) estimated abundance fractions more accurately than the FCLS for most of panel pixels. Nevertheless, the  $\mathbf{S}_W^{-1}$ -weighted AC-LSMA by (c) was still the best shown by Fig. 12 in terms of quantifying abundance fractions of panel pixels.

A remark on the threshold used for the SAM is noteworthy. This threshold was selected empirically for the SAM in our experiments. It was based on our experience working on laboratory and real data. Since laboratory data are generally used for simulations, its tolerance to the threshold is more robust

TABLE II  
SUMMARY OF UNWEIGHTED AC-LSMA (FCLS)  
AND FOUR WEIGHTED AC-LSMA METHODS

	weighting matrix	training samples	signature matrix	undesired signature matrix U
Un-weighted AC-LSMA (FCLS)	$\mathbf{I}$	no	yes	no
MD-weighted AC-LSMA	$\mathbf{K}^{-1}$	no	yes	no
LCMV-weighted AC-LSMA	$\mathbf{R}^{-1}$	no	yes	no
$\mathbf{S}_W^{-1}$ -weighted AC-LSMA	$\mathbf{S}_W^{-1}$	yes	yes	no
OSP-weighted AC-LSMA	$\mathbf{P}_U^\perp$	no	yes	yes

than real data. So, the threshold selected for simulations can be higher than that chosen for real data. Nevertheless, the interval of [0.03, 0.05] for simulated data and the interval of [0.02, 0.03] for real data seem reasonable ranges from which a threshold can be selected. As for the threshold used by the SAM to find undesired signatures for the OSP-weighted LSMA, it was set to 0.06 which is a little bit higher than the thresholds used to find endmembers. This was because undesired signatures were not necessarily as subtle as endmembers. Nonetheless, the selection threshold is generally sensitive to spectral characteristics of signatures to be analyzed. It is advised that several trials of selecting different values in this range may be worthwhile.

As a concluding comment, despite the fact that the  $\mathbf{S}_W^{-1}$ -weighted AC-LSMA was shown to be the best among the six evaluated methods, it requires a good set of training samples to produce the within-class matrix  $\mathbf{S}_W$ . If the sample pool is not well representative like Example 3, it will not perform effectively. On the contrary, if the training samples are selected judiciously as the way was done in Example 4, the  $\mathbf{S}_W^{-1}$ -weighted AC-LSMA will be one of best AC-LSMA methods. Finally, the threshold values used in our experiments for SAM were not optimal, but rather empirical selections.

## V. CONCLUSION

Abundance-constrained linear spectral mixture analysis using the least squares error as a criterion has been studied extensively in the literature. It is generally referred to as least squares AC-LSMA. However, including a weighting matrix in the least squares AC-LSMA to account for significance of individual bands has not been explored in the past years. This paper investigates weighted least squares AC-LSMA and further develops three approaches to weighted least squares AC-LSMA, each of which can be obtained by the commonly used criteria, Mahalanobis distance or Gaussian maximum-likelihood estimation, Fisher's ratio and orthogonal subspace projection. In particular, the least squares AC-LSMA can be considered as an unweighted AC-LSMA. The experimental results demonstrate that weighted AC-LSMA generally performs better than the unweighted AC-LSMA.

As a concluding remark, we summarize the advantages and disadvantages of the unweighted AC-LSMA (i.e., FCLS) along with all the four weighted AC-LSMA methods considered in this paper in Table II.

## REFERENCES

- [1] C.-I Chang, *Hyperspectral Imaging: Techniques for Spectral Detection and Classification*. New York: Kluwer, 2003.
- [2] J. B. Adams, M. O. Smith, and A. R. Gillespie, "Image spectroscopy: Interpretation based on spectral mixture analysis," in *Remote Geochemical Analysis: Elemental and Mineralogical Composition*, C. M. Pieters and P. A. Englert, Eds. Cambridge, U.K.: Cambridge Univ. Press, 1993, pp. 145–166.
- [3] D. E. Sabol, J. B. Adams, and M. O. Smith, "Quantitative sub-pixel spectral detection of targets in multispectral images," *J. Geophys. Res.*, vol. 97, pp. 2659–2672, 1992.
- [4] E. A. Ashton and A. Schaum, "Algorithms for the detection of sub-pixel targets in multispectral imagery," *Photogramm. Eng. Remote Sens.*, vol. 64, no. 7, pp. 723–731, Jul. 1998.
- [5] C.-I Chang and D. Heinz, "Constrained subpixel detection for remotely sensed images," *IEEE Trans. Geosci. Remote Sens.*, vol. 38, no. 3, pp. 1144–1159, May 2000.
- [6] J. B. Adams and M. O. Smith, "Spectral mixture modeling: A new analysis of rock and soil types at the Viking Lander 1 suite," *J. Geophys. Res.*, vol. 91, no. B8, pp. 8098–8112, Jul. 10, 1986.
- [7] J. B. Adams, M. O. Smith, and A. R. Gillespie, "Simple models for complex natural surfaces: A strategy for hyperspectral era of remote sensing," in *Proc. IGARSS*, 1989, pp. 16–21.
- [8] J. C. Harsanyi and C.-I Chang, "Hyperspectral image classification and dimensionality reduction: An orthogonal subspace projection approach," *IEEE Trans. Geosci. Remote Sens.*, vol. 32, no. 4, pp. 779–785, Jul. 1994.
- [9] C.-I Chang, X. Zhao, M. L. G. Althouse, and J.-J. Pan, "Least squares subspace projection approach to mixed pixel classification in hyperspectral images," *IEEE Trans. Geosci. Remote Sens.*, vol. 36, no. 3, pp. 898–912, May 1998.
- [10] M. Brown, H. G. Lewis, and S. R. Gunn, "Linear spectral mixture models and support vector machines for remote sensing," *IEEE Trans. Geosci. Remote Sens.*, vol. 38, no. 5, pp. 2346–2360, Sep. 2000.
- [11] A. F. H. Goetz and J. W. Boardman, "Quantitative determination of imaging spectrometer specifications based on spectral mixing models," in *Proc. IGARSS*, 1989, pp. 1036–1039.
- [12] Y. E. Shimabukuro and J. A. Smith, "The least-squares mixing models to generate fraction images derived from remote sensing multispectral data," *IEEE Trans. Geosci. Remote Sens.*, vol. 29, no. 1, pp. 16–20, Jan. 1991.
- [13] J. J. Settle and N. A. Drake, "Linear mixing and estimation of ground cover proportions," *Int. J. Remote Sens.*, vol. 14, no. 6, pp. 1159–1177, 1993.
- [14] M. O. Smith, D. A. Roberts, J. Hill, W. Mehl, B. Hosgood, J. Verdebout, G. Schmuck, C. Koechler, and J. B. Adams, "A new approach to quantifying abundances of materials in multispectral images," in *Proc. IGARSS*, Pasadena, CA, 1994, pp. 2372–2374.
- [15] S. Tompkins, J. F. Mustard, C. M. Pieters, and D. W. Forsyth, "Optimization of targets for spectral mixture analysis," *Remote Sens. Environ.*, vol. 59, pp. 472–489, 1997.
- [16] D. Heinz and C.-I Chang, "Fully constrained least squares linear mixture analysis for material quantification in hyperspectral imagery," *IEEE Trans. Geosci. Remote Sens.*, vol. 39, no. 3, pp. 529–545, Mar. 2001.
- [17] N. Keshava and J. F. Mustard, "Spectral unmixing," *IEEE Signal Process. Mag.*, vol. 19, no. 1, pp. 44–57, Jan. 2002.
- [18] C. Wu and A. T. Murray, "Estimating impervious surface distribution by spectral mixture analysis," *Remote Sens. Environ.*, vol. 84, pp. 493–505, 2003.
- [19] C.-I Chang, H. Ren, C.-C. Chang, J. O. Jensen, and F. D'Amico, "Estimation of subpixel target size for remotely sensed imagery," *IEEE Trans. Geosci. Remote Sens.*, vol. 42, no. 6, pp. 1309–1320, Jun. 2004.
- [20] C.-I Chang, "Orthogonal subspace projection revisited: A comprehensive study and analysis," *IEEE Trans. Geosci. Remote Sens.*, 2005, submitted for publication.
- [21] K. Fukunaga, *Statistical Pattern Recognition*, 2nd ed. New York: Academic, 1992.
- [22] J. J. Settle, "On the relationship between spectral unmixing and subspace projection," *IEEE Trans. Geosci. Remote Sens.*, vol. 34, no. 4, pp. 1045–1046, Jul. 1996.
- [23] C.-I Chang, "Target signature-constrained mixed pixel classification for hyperspectral imagery," *IEEE Trans. Geosci. Remote Sens.*, vol. 40, no. 5, pp. 1065–1081, May 2002.
- [24] R. E. Duda and P. E. Hart, *Pattern Classification and Scene Analysis*. New York: Wiley, 1973.
- [25] B. Ji, C.-I Chang, J. O. Jensen, and J. L. Jensen, "Unsupervised constrained linear Fisher's discriminant analysis for hyperspectral image classification," in *49th Annu. Meeting, SPIE Int. Symp. Optical Science and Technology, Imaging Spectrometry IX (AM105)*, Denver, CO, Aug. 2–4, 2004.
- [26] C.-I Chang and B. Ji, "Fisher's linear spectral mixture analysis," *IEEE Trans. Geosci. Remote Sens.*, 2005, accepted for publication.
- [27] Q. Du and C.-I Chang, "A signal-decomposed and interference-annihilated approach to hyperspectral target detection," *IEEE Trans. Geosci. Remote Sens.*, vol. 42, no. 4, pp. 892–906, Apr. 2004.
- [28] L. L. Scharf, *Statistical Signal Processing*. Reading, MA: Addison-Wesley, 1991.
- [29] H. Ren and C.-I Chang, "Automatic spectral target recognition in hyperspectral imagery," *IEEE Trans. Aerosp. Electron. Syst.*, vol. 39, no. 4, pp. 1232–1249, Oct. 2003.
- [30] T. M. Tu, C.-H. Chen, and C.-I Chang, "A posteriori least squares orthogonal subspace projection approach to weak signature extraction and detection," *IEEE Trans. Geosci. Remote Sens.*, vol. 35, no. 1, pp. 127–139, Jan. 1997.
- [31] C.-I Chang and Q. Du, "Estimation of number of spectrally distinct signal sources in hyperspectral imagery," *IEEE Trans. Geosci. Remote Sens.*, vol. 42, no. 3, pp. 608–619, Mar. 2004.
- [32] M. E. Winter, "N-finder: An algorithm for fast autonomous spectral end-member determination in hyperspectral data," in *Proc. SPIE Conf. Image Spectrometry V*, vol. 3753, 1999, pp. 266–277.



**Chein-I Chang** (S'81–M'87–SM'92) received the B.S. degree from Soochow University, Taipei, Taiwan, R.O.C., in 1973, the M.S. degree from the Institute of Mathematics, National Tsing Hua University, Hsinchu, Taiwan, in 1975, and the M.A. degree from the State University of New York, Stony Brook, in 1977, all in mathematics. He received the M.S. and M.S.E.E. degrees from the University of Illinois at Urbana-Champaign in 1982 and the Ph.D. degree in electrical engineering from the University of Maryland, College Park, in 1987.

He has been with the University of Maryland Baltimore County (UMBC), Baltimore, since 1987, as a Visiting Assistant Professor from January 1987 to August 1987, Assistant Professor from 1987 to 1993, Associate Professor from 1993 to 2001, and Professor in the Department of Computer Science and Electrical Engineering since 2001. He was a Visiting Research Specialist in the Institute of Information Engineering at the National Cheng Kung University, Tainan, Taiwan, from 1994 to 1995. He has three patents on automatic pattern recognition and several pending patents on image processing techniques for hyperspectral imaging and detection of microcalcifications. His research interests include multispectral/hyperspectral image processing, automatic target recognition, medical imaging, information theory and coding, signal detection and estimation, and neural networks. He is the author of a book *Hyperspectral Imaging: Techniques for Spectral Detection and Classification* (Kluwer). He is on the editorial board and was the Guest Editor of a special issue on telemedicine and applications of the *Journal of High Speed Networks*.

Dr. Chang received a National Research Council Senior Research Associateship Award from 2002 to 2003 at the U.S. Army Soldier and Biological Chemical Command, Edgewood Chemical and Biological Center, Aberdeen Proving Ground, MD. He is an Associate Editor in the area of hyperspectral signal processing for the IEEE TRANSACTIONS ON GEOSCIENCE AND REMOTE SENSING. He is a Fellow of SPIE and a member of Phi Kappa Phi and Eta Kappa Nu.



**Baohong Ji** (S'05) received the B.S. and M.S. degrees in computer science from Jilin University of Technology, Jilin, China, in 1993 and 1996, respectively. She is currently pursuing the Ph.D. degree at the University of Maryland Baltimore County, Baltimore.

From 1997 to 2000, she served as a Lecturer in Jilin University of Technology. Her research interests include remote sensing, image processing, data compression, and pattern recognition.